Supplementary Information for "Symmorphic intersecting nodal rings in semiconducting layers"

Cheng Gong,[1] Yuee Xie,[1] Yuanping Chen,[1] Heung-Sik Kim,[2] and David Vanderbilt[2]

[1]*School of Physics and Optoelectronics, Xiangtan University, Xiangtan, 411105, Hunan, China*

[2]*Department of Physics and Astronomy, Rutgers University, Piscataway, New Jersey 08854-8019, USA*

CONTENTS

I. BAND REPRESENTATION ANALYSES FOR LAYERED AND BUCKLED HONEYCOMB STRUCTURES

A. An introduction to band representation analysis

Here we denote nodal rings touching each other as *intersecting nodal rings* (INRs), rings winding each other as *Hopf links*, and those with neither intersecting nor forming Hopf links as *separate nodal rings*. In the INR case, the point where the two nodal line cross will be denoted as the *nodal intersecting point*. Also, we use 'IRREP' as a shorthand notation for 'irreducible representation.'

In the manuscript we showed that INRs can exist when there are two (or more) mirror planes intersecting each other, so that the nodal intersecting point exists on the mirror-intersecting line. This suggests that we may also have additional INRs with nodal intersecting points located on the other mirror-intersecting line Γ-Y (see Fig. 3(d-f) in the manuscript for the special points notation), which were not found in the tight-binding and *ab-initio* calculations. It can be seen that, by employing a *band representation* (BR) analysis, nodal intersecting points can exist only on the Z-T line when we are considering only the p_z-orbitals at sp^2-bonded sites, so that our listing of INR structures in Fig. 3 covers all possible INR cases. This is because the *symmetries of the local orbitals underlying the band structure determines the kind and number of IRREPs in the entire momentum space.*

Before describing these results, we describe below what a BR analysis is in a hand-waving manner. For a mathematically rigorous presentation please refer to Refs. 1–4 and references therein.[5] Basically, it is a momentum-space representation of a space group. We know well about the representation theory of little co-groups (which are point groups) at high-symmetry k-points, which tells us how many different kinds of degenerate states (*i.e.*, IRREPs) we can have for each k-point. On the other hand, from the number of local orbitals and number of sites in our choice of unit cell, we know how many bands we will have in our tight-binding model. BR theory is, roughly speaking, the combination of these two ideas; choosing our set of sites and local orbitals from which we will construct our model, we can explicitly write the the representation of each space group operation in terms of a local-orbital basis in real space (which becomes an infinite-dimensional unitary matrix) and then do the Fourier transform to obtain a k-space representation. Among the original space-

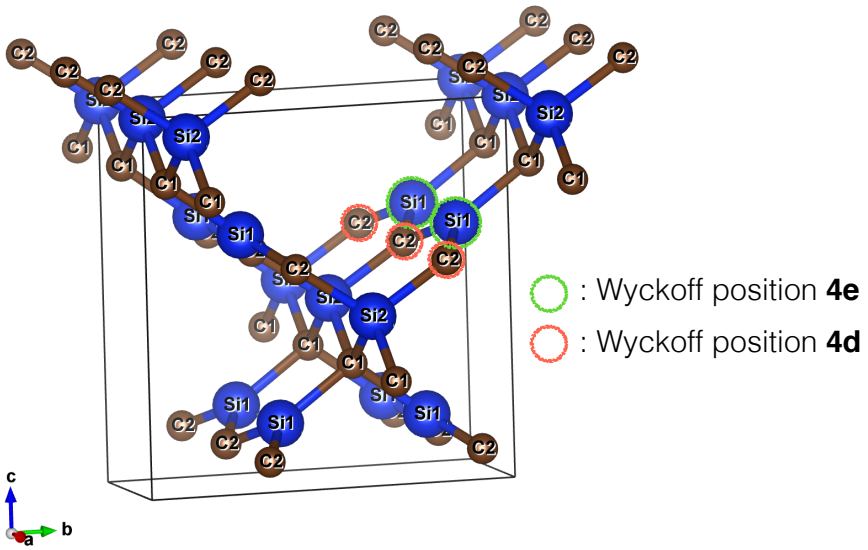

FIG. S1. (color online) Crystal structrue of buckled honeycomb SiC with $Amm2$ space group. p_z-like orbitals at Si1 and C2 sites, highlighted with green (Wyckoff position 4e) and pink (4d) circles respectively, contributes to the bands near the Fermi level.

group operations, we can choose a little group of a lower-symmetry k-point (*i.e.*, 'subducing' the representation) and find which kind of IRREPs we have at that point. Furthermore, for any high-symmetry lines connecting two points with even higher symmetry, we can find '*compatibility relations*' telling us about how each IRREP on one higher-symmetry point is connected to IRREPs on another point through the line connecting the two points. From this analysis the connectivity of high-symmetry IRREPs to form a band structure can be obtained, and the nodal ring structure can also be deduced.

B. Choice of local orbitals in buckled honeycomb SiC (space group $Amm2$)

Below we apply the BR theory to a simple example, the buckled honeycomb SiC with the $Amm2$ space group symmetry discussed in the manuscript. Note that the BR analysis employed in this $Amm2$ example can be applied to the layered honeycomb structure with the $Cmmm$ symmetry to yield the same conclusion as presented in Sec. I E. Here we do not consider the effect of SOC, which gaps out all nodal lines and drives the system either to a weak or strong topological insulator.[6] Fig. S1 shows the crystal structure of SiC with $Amm2$ symmetry in a conventional setting, where there are two mirror planes perpendicular to **a** (denoted $m_{\rm A}$) and to **b** ($m_{\rm B}$). In the primitive cell there are four different symmetry-

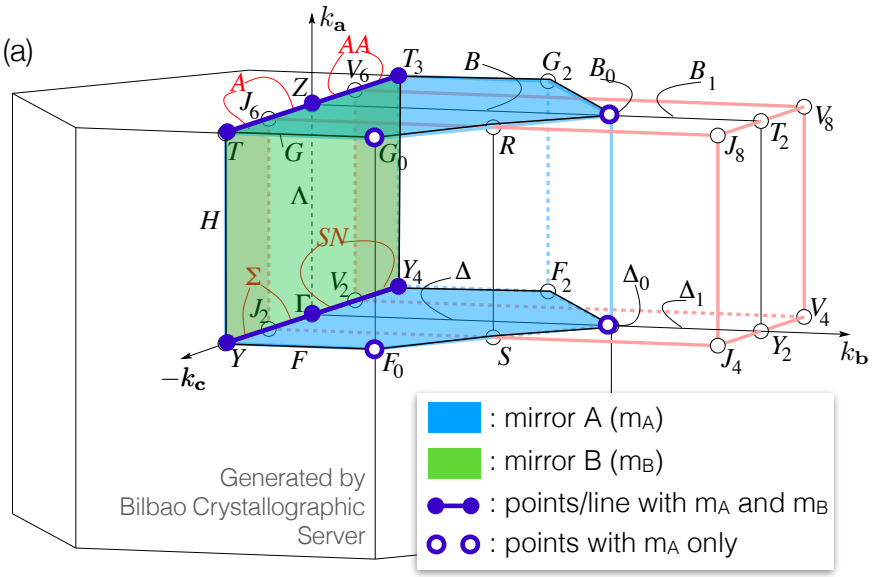

(b) from C2 (WP 4d)

Band-Rep.	A'↑G(2)
Band-type	Composite
Z:(1/2,0,0)	$Z_1(1) \oplus Z_4(1)$
T:(1/2,0,-1)	$T_1(1) \oplus T_4(1)$
R:(1/2,1/2,-1/2)	$2\,R_1(1)$
S:(0,1/2,-1/2)	$2\,S_1(1)$
Y:(0,0,-1)	$Y_1(1) \oplus Y_4(1)$
Γ:(0,0,0)	$Γ_1(1) \oplus Γ_4(1)$

(c) from Si1 (WP 4e)

Band-Rep.	A'↑G(2)
Band-type	Composite
Z:(1/2,0,0)	$Z_2(1) \oplus Z_3(1)$
T:(1/2,0,-1)	$T_2(1) \oplus T_3(1)$
R:(1/2,1/2,-1/2)	$2\,R_2(1)$
S:(0,1/2,-1/2)	$2\,S_1(1)$
Y:(0,0,-1)	$Y_1(1) \oplus Y_4(1)$
Γ:(0,0,0)	$Γ_1(1) \oplus Γ_4(1)$

Tables generated by BANDREP in Bilbao Crystallographic Server

FIG. S2. (color online) (a) Brillouin zone and high-symmetry planes of $Amm2$ structure, where $m_{\rm A}$ and $m_{\rm B}$ are perpendicular to the **a** and **b** axes in Fig. 1 respectively. Note that B_0, G_0, Δ_0, and F_0 has only $m_{\rm A}$ symmetry. (b,c) Tables of BRs generated from Wyckoff position 4d (b) and 4e (c). Note that C2 (shown in Fig. 1) and Si1 are located at 4d and 4e sites respectively. In both tables, grey rectangles highlight BRs induced from p_z-like orbitals (A' IRREP of C_s site symmetry, symmetric upon $m_{\rm A}$ operation, at both 4d and 4e sites).

inequivalent sites: C1 and Si2 with C_{2v} site symmetry, and C2 and Si1 with lower C_s symmetry associated with $m_{\rm A}$ only. Since C1 and Si2 sites are sp^3-bonded, we choose instead to explore the bands induced from the p_z-like orbitals at the C2 and Si1 sites, which are nearer to the Fermi level.

To construct the BRs, we start from the p_z-like orbitals (A' IRREP, symmetric upon $m_{\rm A}$)

at C2 and Si1 sites with C_s point group symmetry. Using the BANDREP program recently implemented in the Bilbao Crystallographic Server,[7,8] we can generate BRs as shown in Fig. S2(b) and (c). In the tables, the first row shows which local IRREP we chose to construct the BR. Here we are interested in bands consisting of A' IRREP (p_z-like orbitals) at 4d (b) and 4e (c) Wyckoff sites. The 'composite' band-type in the second row means that the two bands generated can be separated into two 'elementary' sets of BRs with a constant energy shift of each subband, where elementary BRs (EBRs) are defined as BRs induced from IRREPs at Wyckoff positions with maximal site symmetry. In spinless systems it has been shown that EBRs are indecomposable,[9,10] *i.e.* an EBR cannot be decomposed into two sets of smaller BRs separated by a band gap. Note that $Amm2$ symmetry allows only one-dimensional EBRs in the absence of spin. Lastly, the third and subsequent rows in the tables show which IRREPs exist at six high-symmetry points (Z, T, R, S, T, and Γ), where the BZ and high-symmetry k-points are shown in Fig. S2(a). Note that the Z-T and Γ-Y lines are mirror-intersecting lines with C_{2v} symmetry, so they can host four one-dimensional IRREPs $\{\mathrm{Z,T,Y,\Gamma}\}_{1,\cdots,4}$, while points R and S have only two IRREPs $\{\mathrm{R,S}\}_{1,2}$ from their C_s symmetry. Also note that, in Fig. S2(a), point R (S) has the same symmetry with B_0 and G_0 (Δ_0 and F_0).

C. Compatibility relation between high-symmetry k-points

Since we know how many different IRREPs we have in our system, we now need to connect them to form the band structures. BANDREP provides the information about the connectivity (i.e., the compatibility relations), so that one can simply use them, but here we want to be a bit more illustrative. The compatibility relations between different IRREPs is determined by how IRREPs at higher-symmetry points are reduced into IRREPs with lower symmetries, deduced from their symmetry eigenvalues. Eigenvalues of m_{A} and m_{B} for each

IRREP at different k-points are as follows;

	m_{A}	m_{B}
$\{Z,T,Y,\Gamma\}_1$	$+$	$+$
$\{Z,T,Y,\Gamma\}_2$	$-$	$-$
$\{Z,T,Y,\Gamma\}_3$	$-$	$+$
$\{Z,T,Y,\Gamma\}_4$	$+$	$-$
$\{B_0,G_0,\Delta_0,F_0\}_1$	$+$	$\cdot$
$\{B_0,G_0,\Delta_0,F_0\}_2$	$-$	$\cdot$
Λ_1	$\cdot$	$+$
Λ_2	$\cdot$	$-$

(S1)

where Λ denotes a generic point on the m_{B} plane in Fig. S2(a). From this, we know that $\{\mathrm{Z,T,Y,\Gamma}\}_{1,4}$ are connected to $\{\mathrm{B_0,G_0,\Delta_0,F_0}\}_1$ and $\{\mathrm{Z,T,Y,\Gamma}\}_{2,3}$ to $\{\mathrm{B_0,G_0,\Delta_0,F_0}\}_2$ when we deviate from the mirror-intersecting line but stay in the m_{A} plane. Similarly, $\{\mathrm{Z,T,Y,\Gamma}\}_{1,3}$ and $\{\mathrm{Z,T,Y,\Gamma}\}_{2,4}$ are connected to Λ_1 and Λ_2, respectively, in the m_{B} plane.

D. Possible band structures and nodal lines in SiC

Now we are ready to generate possible set of band structures from the sp^2-bonded sites in buckled SiC. A couple of remarks are worth mentioning for further simplification of our analysis; *i)* Unlike other high-symmetry points, the points on the m_{A} plane with $k_x = 0$ (represented by S) host only a single IRREP S_1 as shown in Fig. S2(b) and (c), implying we do not have any protected band crossing on the plane. *ii)* From the symmetry argument in the manuscript, we know that nodal intersecting points can only happen on the mirror-intersecting lines and when two IRREPs with two opposite eigenvalues cross each other. Denoting the IRREPs at generic k-points on the mirror-intersecting Z-T and Γ-Y lines as $\overline{\mathrm{ZT}}_{1,\cdots,4}$ and $\overline{\Gamma\mathrm{Y}}_{1,\cdots,4}$, respectively, we can have nodal intersecting points when $\{\overline{\mathrm{ZT}},\overline{\Gamma\mathrm{Y}}\}_1$ and $\{\overline{\mathrm{ZT}},\overline{\Gamma\mathrm{Y}}\}_2$ (or $\{\overline{\mathrm{ZT}},\overline{\Gamma\mathrm{Y}}\}_3$ and $\{\overline{\mathrm{ZT}},\overline{\Gamma\mathrm{Y}}\}_4$) cross on the mirror-intersecting lines. While we have all four IRREPs on the Z-T line, on the contrary, we have only two IRREPs $\overline{\Gamma\mathrm{Y}}_{1,4}$ on the Γ-Y line, implying that we cannot have nodal intersecting points on the Γ-Y line. This is a crucial distinction between the two mirror-intersecting lines that will have important

consequences shortly.

With the IRREPs at high-symmetry points in Fig. S2 and the compatibility relations in Table (S1), the qualitative nature of the band dispersion is determined by the energy ordering of IRREPs. Assuming for simplicity that the dispersions are monotonic along a line segment connecting two high-symmetry points in the BZ, the band structure is determined by energy ordering of IRREPs at six k-points, Z, T, Y, Γ, B_0, and G_0 (since no crossing can exist on the m_A plane with $k_{\mathbf{a}}$, the plane containing the S point). Because there are four 1D IRREPs at Z and T, two 1D IRREPs at Y, Γ, B_0, and G_0, and four bands in total, the number of all possible band structures are $(4!)^2 \left(\frac{4!}{2^2}\right)^4 = 746496$, so generating all of the bands is neither possible nor necessary. Hence, below we will discuss a few illustrative examples about how different kinds of nodal ring structures (separated, INR, and Hopf link) can be generated from our 4-band model. Note that similar but more elaborate analysis was done by Bouhon and Black-Schaffer for space group $Pna2_1$ (SG #33),[11] where the number of possible band structures is greatly reduced by the degeneracy enforced by the three perpendicular screw axes.

1. *NLs involving two bands*

First we consider situations with only two bands crossing at the Fermi level. For simplicity, here we assume that the other two bands are away from the Fermi level (one occupied, another unoccupied) and do not cross with others as shown in Fig. S3. Hereafter we consider half-filling (2 bands occupied), and because we have time-reversal (TR) symmetry, only high-symmetry planes and lines in the TR-irreducible section in the BZ will be depicted.[12]

Fig. S3(a) shows bands with NL crossing on the m_B plane. Here we are depicting bands contributing and not contributing to the NLs as solid and dotted lines, respectively. In Fig. S3(a), we chose that only bands induced from the 4d Wyckoff position (C2) are crossing near the Fermi level, while the bands from the 4e sites (Si1) are away from the Fermi level. Note that when we are making only the solid bands cross, we may have NLs only on the m_B plane since $\{\overline{\mathrm{ZT}},\overline{\Gamma\mathrm{Y}}\}_{1,4}$ have the same m_A eigenvalue. Since no degeneracy is enforced at any k-points, the open NL can be freely deformed into a closed nodal ring or even be removed without any symmetry breaking. Similarly, it is easy to see that we get an identical result when we have two bands from the 4e sites near the Fermi level.

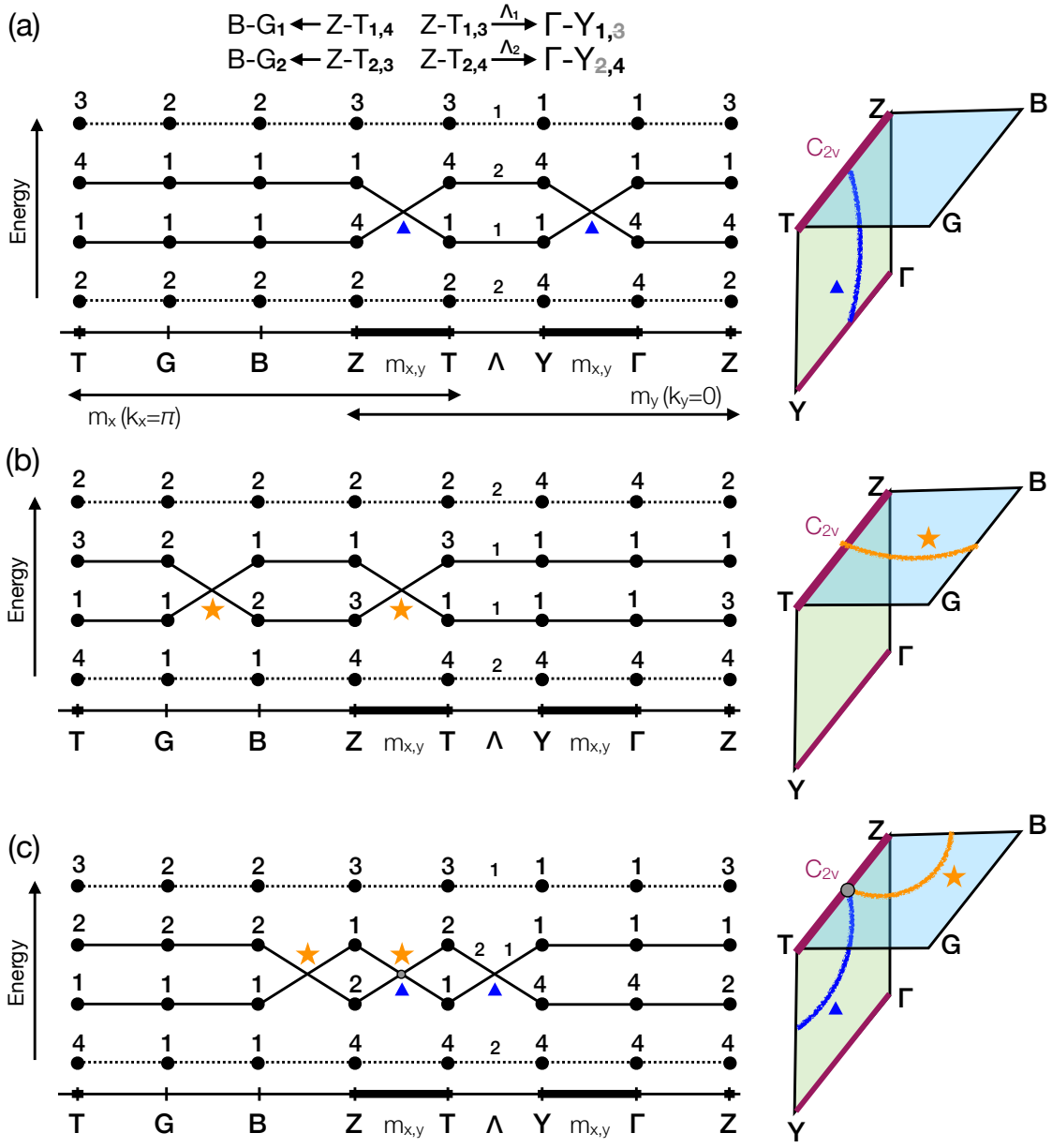

FIG. S3. (color online) Three examples of band structures with two bands contributing to the NLs, where (a) shows the bands induced from 4d (C2) sites near the Fermi level with an open NL on the m_{B} plane as shown in the right panel, while in (b) one band from 4d and another from 4e (Si1) is crossing to form a NL on the m_{B} plane. Note that the NLs can be closed to form nodal rings by inverting bands on the mirror planes. (c) shows the β-type INR, which can be transformed to α-type, or crossing of two open NLs. Note that the nodal intersecting point is marked with grey circle. In the left panels, numbers represent IRREPs at each k-points, and dotted lines depict bands not contributing to the NLs. Band crossings, giving rise to the NLs in the right panels (blue and orange lines), are marked with blue triangles and orange stars.

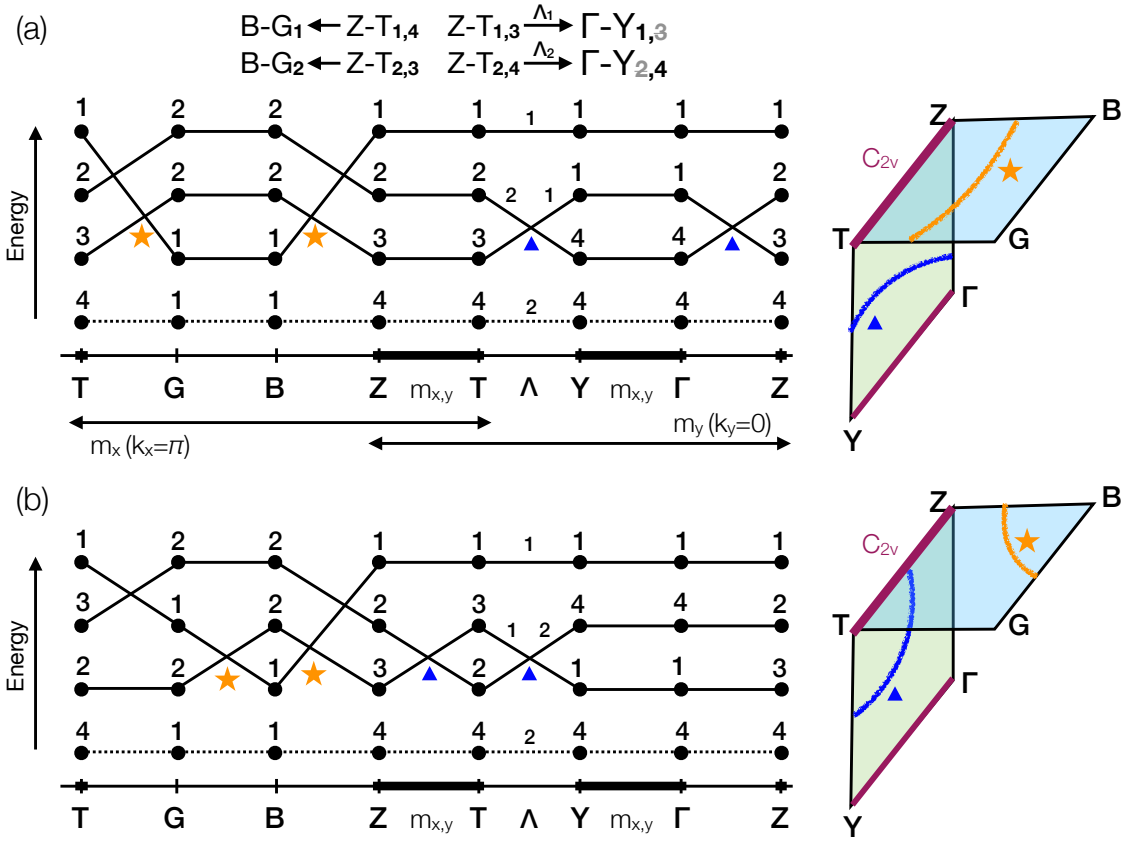

FIG. S4. (color online) Two examples of NLs with three bands, where the two NLs are not sharing the mirror-intersecting Z-T line. (a) Two open NLs, and (b) two nodal rings.

Fig. S3(b) and (c) show the band crossings, choosing one 4d-induced band and another from 4e-induced ones. Fig. S3(b) shows bands with a NL only on the $m_{\rm A}$ plane, while Fig. S3(c) shows the β-type INR. By comparing Fig. S3(a-c), we can see that the mirror eigenvalues of the IRREPs crossing on the mirror-intersecting Z-T line determines the presence of NLs on each mirror plane, as discussed above and in the manuscript.

2. NLs involving three bands

Now we discuss the band crossings involving three bands. As shown in Fig. S4, we can introduce two separate NLs without sharing the mirror-intersecting Z-T line by combining band crossings depicted in Fig. S3(a) and (b). On the contrary, when we want to make the two NLs share the mirror intersecting line to form INR or Hopf link, as shown in Fig. S5, then we need to cross IRREPs with two opposite eigenvalues on the Z-T line ($\overline{\rm ZT}_1$ and $\overline{\rm ZT}_2$, or $\overline{\rm ZT}_3$ and $\overline{\rm ZT}_4$). We mention that, this condition is similar with the one presented in Ref.

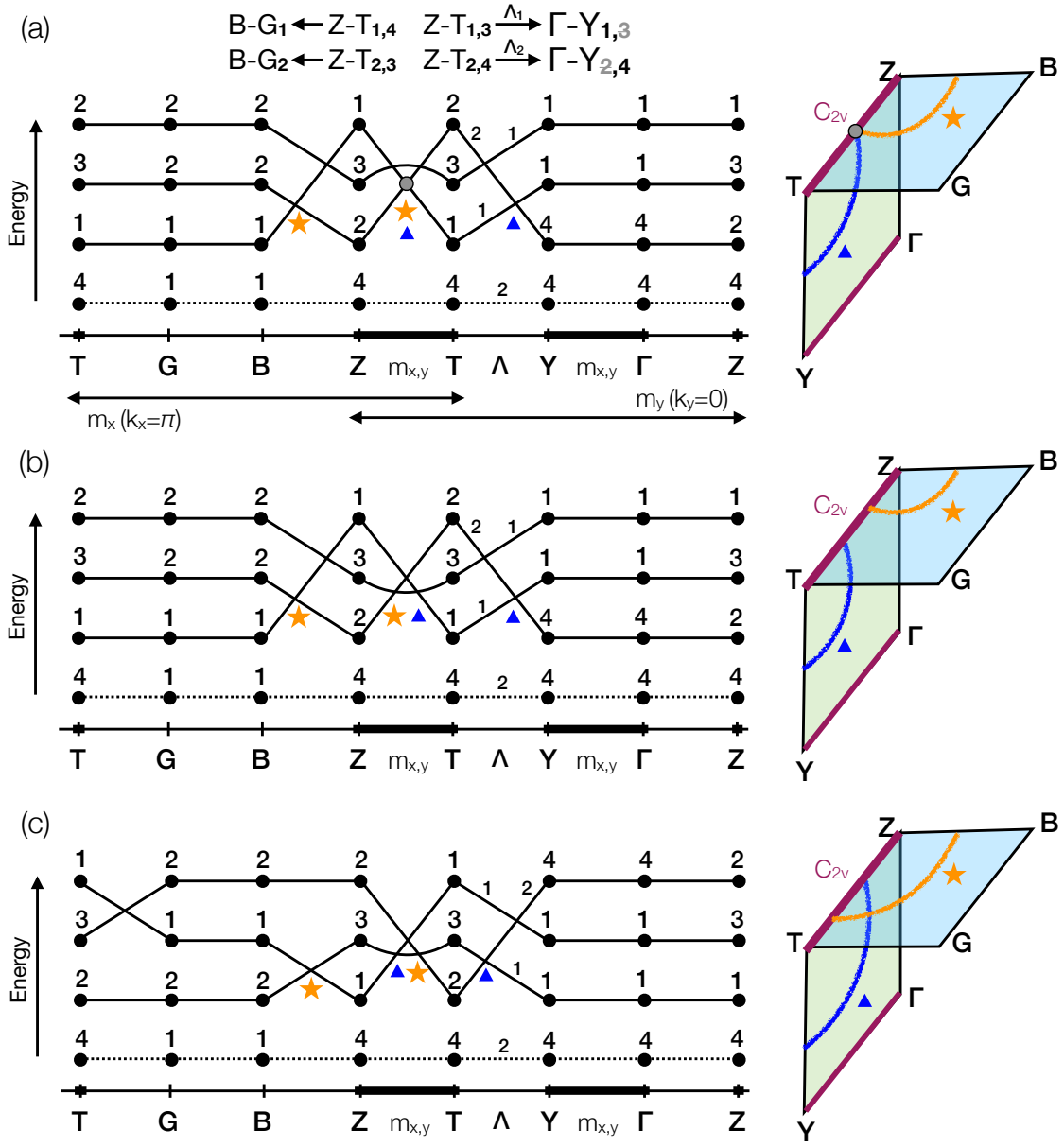

FIG. S5. (color online) Three examples of 3-band-NLs sharing the mirror-intersecting line, where one can have (a) INR, (b) two separate nodal rings, and (c) Hopf link. Note that (a) is actually equivalent to the INR depicted in Fig. S3(c), except the band inversion between $Z_{1,3}$ and $T_{2,3}$ in the unoccupied bands. The nodal intersecting point splits into two separate nodal lines as the $\{Z,T\}_3$ band moves down and is occupied, as shown in (b). (c) shows an example of Hopf link from crossings of three bands. Note that unlike the transition from (a) and (b), transition from (a) (or from (b)) to (c) requires global change of band ordering in the k-space.

13, where the transformation of two separate nodal rings into a Hopf link is shown in a four-band model with three distinct IRREPs on the mirror-intersecting line. Unlike their model, however, in Fig. S5 we are considering situations with only three bands with distinct

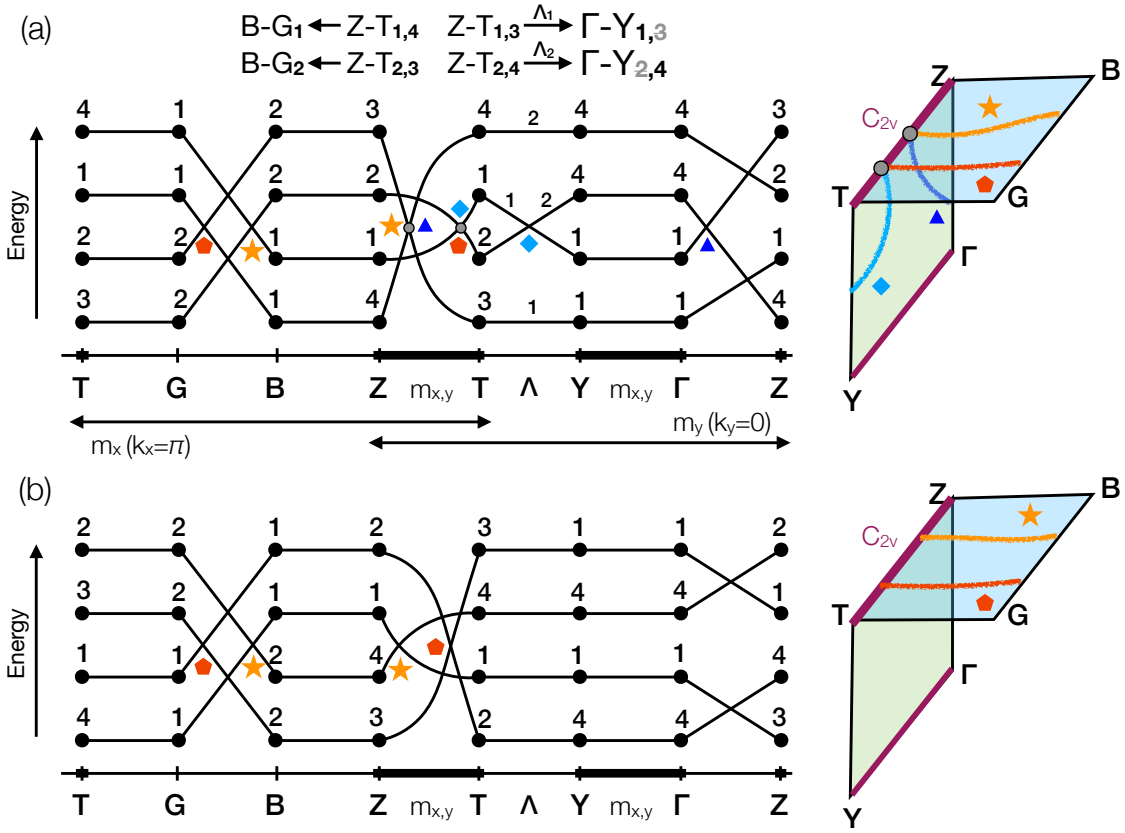

FIG. S6. (color online) Two examples of NLs involving four bands. (a) shows bands with two nodal intersecting points on the Z-T line, which corresponds to the γ-type INR in the manuscript. (b) shows two nodal lines on the $m_{\rm A}$-plane. Note that we can also have two nodal rings on the $m_{\rm A}$-plane by exchanging IRREPs on the Z-T line.

IRREPs are crossing on the mirror-intersecting line. Because of this, it is not possible to transform two separate NLs into a Hopf link by inverting bands only on the Z-T line, which is evident by comparing Fig. S5 (b) and (c).

3. NLs involving four bands

Finally we discuss situations where all the 4 bands are contributing to the NL crossings. Fig. S6(a) shows the γ-type nodal intersecting points, while Fig. S6(b) depicting two NLs on the $m_{\rm A}$ plane. Note that both in Fig. S6(a) and (b), by shifting the NL crossing points on the Z-T line, they can overlap at a same point so that all the NLs (4 in (a), 2 in (b)) are connected. However this is just an accidental crossing by a fine-tuning of parameters so may not be physically relevant.

E. Band representations for layered honeycomb (space group $Cmmm$)

In the manuscript, we discuss the layered honeycomb structures with the $Cmmm$ space group in addition to the buckled honeycomb structures. Because the inversion symmetry is present in $Cmmm$ in addition to all the operations in $Amm2$, it has three mirror planes perpendicular to each other. Since there exist more mirror-intersecting lines in the momentum space compared to the $Amm2$ structure, we might have additional nodal intersecting points on different mirror-intersecting lines to form even more complicated nodal structures. Inducing the band representation from the p_z orbitals at each site and looking into the allowed IRREPs on the lines, however, it turns out that there is only one line, the Z-T line, accommodating IRREPs which can form the nodal intersecting points. Hence the presence of the additional mirror plane in the $Cmmm$ structure (compared to the $Amm2$ one) does not change our conclusion that the three types of INR (α-, β-, and γ-type) exhaust all possible kind of INRs in our layered and buckled honeycomb structures.

II. A $k \cdot p$ MODEL FOR THE THREE TYPES OF INRS

Comparing the four-band TB model in Eq. (1) in the manuscript, we can construct a two-band $k \cdot p$ model to further compare the INRs. All the three types of INRs have a common nodal ring centered on the point T (see Figs. 3(d-f) in the manuscript). Constrained by the symmetries and the time reversal symmetry for a spinless system, one obtains a model up to quadratic order in k around T as

$$H(\mathbf{q}) = \begin{pmatrix} A_1 q_x^2 + B_1 q_y^2 + C_1 q_z^2 & -iDq_xq_y \\ iDq_xq_y & \Delta + A_2 q_x^2 + B_2 q_y^2 + C_2 q_z^2 \end{pmatrix}$$

where $q_i = k_i - k_{i0}$ $(i = x, y, z)$ and (k_{x0}, k_{y0}, k_{z0}) is the momentum coordinate at point T. The parameters Δ, $\{A, B, C\}_{\{1,2\}}$, and D are determined by fitting DFT or TB results. When $\{A, B, C\}_1 > 0$ and $\{A, B, C\}_2 < 0$, it produces an α-type INR; when $A_1, B_2, C_1 > 0$ and $A_2, B_1C_2 < 0$, a β-type-like INR is produced, in which a nodal ring linked two curved nodal lines; when $A_1, C_1 > 0$, $A_2, C_2 < 0$ and $B_1, B_2 = 0$, a γ-type-like INR is produced, where a nodal ring linked two straight nodal lines. Note that we need a find-tuning of B_1 and B_2 parameters to realize the γ-type INR in this two-band model since it generally requires

4 bands.

III. COMPUTATIONAL DETAILS

Our first-principles calculations were based on the density functional theory (DFT) as implemented in the Vienna Ab-initio Simulation Package.[14] The core-valence interactions were described by projector augmented-wave (PAW) potentials within the Perdew-Burke-Ernzerhof (PBE) approximation for the exchange-correlation energy.[15] Plane waves with a kinetic energy cutoff of 500 eV were used as the basis set. We used the conjugate gradient method to optimize the atomic positions, and the energy convergence criterion between two consecutive steps was 10^{-5} eV. The maximum allowed force on the atoms is 10^{-3} eV/Å.

IV. ADDITIONAL SUPPLEMENTARY TABLES AND FIGURES

		θ (Å)	a (Å)	c (Å)	Bond length (Å)	Cohesive energy (eV/atom)
Layered honeycomb structures ($Cmmm$)	BN	64.0	4.424	2.495	1.43-1.70	6.270
	AlP	68.6	6.224	3.926	2.16-2.55	3.303
	GaP	87.9	4.942	3.978	2.10-2.42	2.903
Buckled honeycomb structures ($Amm2$)	SiC	88.9	5.321	3.086	1.77-1.91	6.072
	BP	88.2	5.537	3.193	1.84-1.96	3.606
	BAs	88.1	5.861	3.378	1.95-2.08	2.941

TABLE S1. Structural parameters of the layered and buckled layered structures, consisting of IV or III/V elements. All these structures have topological linked nodal rings.

	θ (deg)	$\epsilon_{1,2}$	$\epsilon_{3,4}$	t_1	t_2	t_3	t_4	t_5	t_6	t_7
BN	64	1.80	-0.90	-1.10	-0.70	-1.50	-0.05	-0.10	0.45	0.10
SiC	89	1.70	-0.90	-1.00	-0.50	-1.20	0.00	0.00	0.45	0.25
	80 (He)	1.70	-0.90	-1.65	-1.00	-1.00	0.15	0.20	0.12	0.10
	108	1.70	-0.90	-0.20	-0.10	-1.40	0.00	0.00	1.10	0.60

TABLE S2. Tight binding parameters (in eV) in Eq. (1) for fitting the DFT band structures in Figs. 4(b-e) in the manuscript.

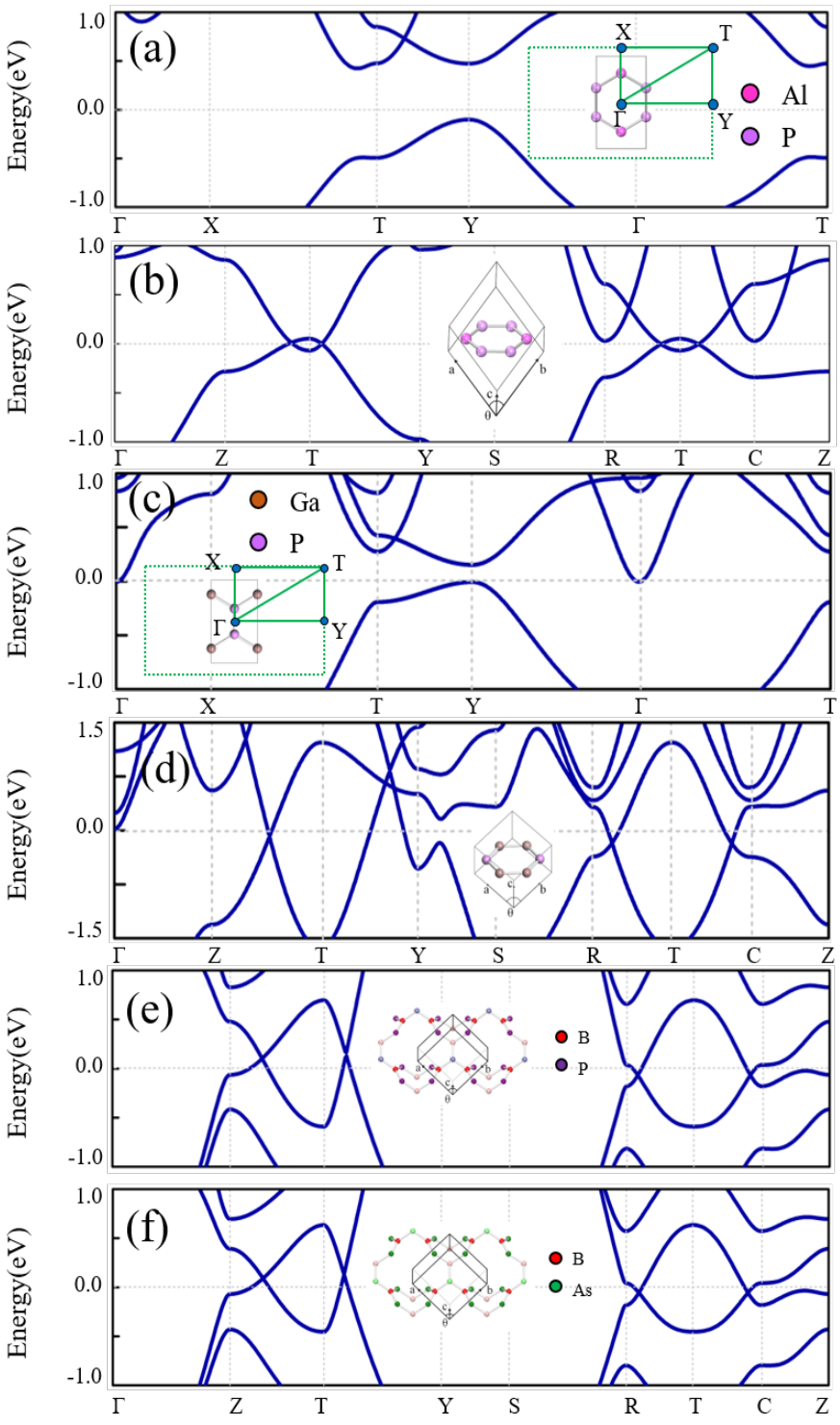

FIG. S7. (color online) Band structures for (a) single-layer AlP, (b) layered 3D AlP, (c) single-layer GaP (d) layered 3D GaP, (e) buckled layered 3D BP and (f) buckled layered 3D BAs.

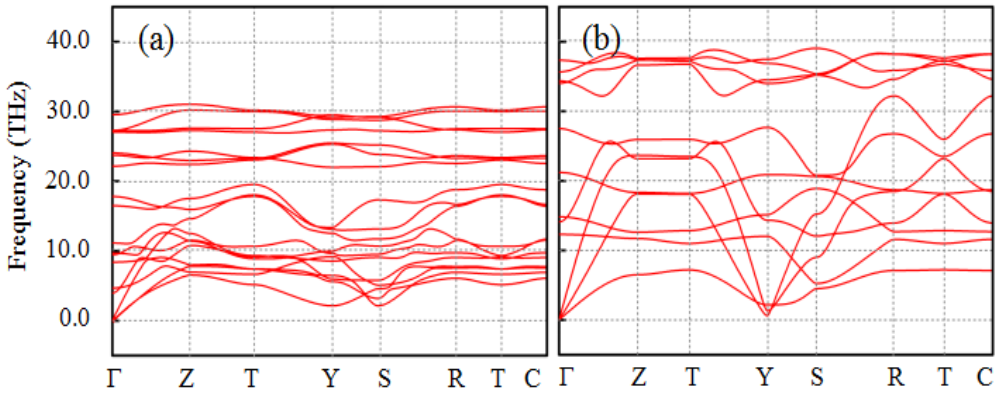

FIG. S8. Phonon dispersions for (a) the buckled layered 3D SiC structure, (b) layered 3D BN structure.

---

[1] B. Bradlyn, L. Elcoro, J. Cano, M. G. Vergniory, Z. Wang, C. Felser, M. I. Aroyo, and B. A. Bernevig, Nature **547**, 298 EP (2017).

[2] M. G. Vergniory, L. Elcoro, Z. Wang, J. Cano, C. Felser, M. I. Aroyo, B. A. Bernevig, and B. Bradlyn, Phys. Rev. E **96**, 023310 (2017).

[3] B. Bradlyn, L. Elcoro, M. G. Vergniory, J. Cano, Z. Wang, C. Felser, M. I. Aroyo, and B. A. Bernevig, arXiv preprint arXiv:1709.01937 (2017).

[4] J. Cano, B. Bradlyn, Z. Wang, L. Elcoro, M. G. Vergniory, C. Felser, M. I. Aroyo, and B. A. Bernevig, arXiv preprint arXiv:1709.01935 (2017).

[5] Note that original studies of BR and their mathematical formulation were done by J. Zak, H. Bacry, and L. Michel for spinless electrons.[9,10] Recent works[1–4] are generalization of the original theory to spinful systems and their utilization in finding topologically nontrivial band structures.

[6] Y. Kim, B. J. Wieder, C. L. Kane, and A. M. Rappe, Phys. Rev. Lett. **115**, 036806 (2015).

[7] *http://www.cryst.ehu.es*.

[8] L. Elcoro, B. Bradlyn, Z. Wang, M. G. Vergniory, J. Cano, C. Felser, B. A. Bernevig, D. Orobengoa, G. de la Flor, and M. I. Aroyo, Journal of Applied Crystallography **50**, 1457 (2017).

[9] J. Zak, Phys. Rev. Lett. **45**, 1025 (1980).

[10] H. Bacry, L. Michel, and J. Zak, Phys. Rev. Lett. **61**, 1005 (1988).

[11] A. Bouhon and A. M. Black-Schaffer, arXiv preprint arXiv:1710.04871 (2017).

[12] Note that TR symmetry plays more important role in constraining the form of Hamiltonian and enforcing degeneracy when we have inversion symmetry, spin degrees of freedom, or rotational symmetry more then three-fold.

[13] G. Chang, S.-Y. Xu, X. Zhou, S.-M. Huang, B. Singh, B. Wang, I. Belopolski, J. Yin, S. Zhang, A. Bansil, H. Lin, and M. Z. Hasan, Phys. Rev. Lett. **119**, 156401 (2017).

[14] G. Kresse and J. Hafner, Phys. Rev. B **47**, 558 (1993).

[15] J. P. Perdew, K. Burke, and M. Ernzerhof, Phys. Rev. Lett. **77**, 3865 (1996).